SUPPLEMENTARY MATERIAL

Patient-specific bicuspid aortic valve biomechanics: an imaging integrated fluid-structure interaction approach

Monica Emendi[§], Francesco Sturla[§], Ram P. Ghosh, Matteo Bianchi, Filippo Piatti, Francesca R. Pluchinotta, Daniel Giese, Massimo Lombardi, Alberto Redaelli, Danny Bluestein*

[§] Both authors equally contributed to first authorship

* Address for correspondence: Prof. Danny Bluestein (danny.bluestein@stonybrtook.edu), Department of Biomedical Engineering, Stony Brook University, HSC T9-050, Stony Brook, NY 11794-8084, USA.

A. Grid sensitivity analysis

Grid sensitivity analysis was accomplished according to the Richardson extrapolation, which is the standard method for estimating numerical error in the verification of numerical calculations. To do so, we run the same FSI analysis on three meshes consisting of about 0.4 (coarse mesh), 0.75 (medium mesh) and 1.5 (fine mesh), million hexahedral elements.

Grid Convergence Index (GCI)[1] was calculated for the fine-to-medium and medium-to-coarse grid refinements, as detailed by Craven *et al.* (2009)[2]. The GCI is a measure of how much the variable of interest is different from a theoretical asymptotic numerical value and quantifies how much the calculated variable of interest would change with a further grid refinement.

At this aim, numerical solutions were computed on the fine (f_1), medium (f_2) and coarse (f_3) grids with sharing a constant refinement ratio (r):

$$r \approx \left(\frac{N_1}{N_2}\right)^{\frac{1}{3}} \approx \left(\frac{N_2}{N_3}\right)^{\frac{1}{3}} \approx 1.25$$

where N_i is the number of elements in the ith grid. For each variable of interest, the order of convergence (p) was calculated as:

$$p = \frac{ln\left(\frac{f_3 - f_2}{f_2 - f_1}\right)}{ln(r)}$$

where f_1, f_2 and f_3 represent the variable of interest computed on the fine, medium and coarse grid, respectively. Since three grids were used to determine the observed order of convergence p, a factor of safety (F_s) of 1.25 was assumed. For each grid refinement, the percentage fractional error was computed as:

$$E_1 = \frac{\frac{f_2 - f_1}{f_1}}{r^p - 1} \qquad E_2 = \frac{\frac{f_3 - f_2}{f_2}}{r^p - 1}$$

between the medium and fine grid (E_1), and between the coarse and medium grid (E_2). Finally, the corresponding GCI was computed for each grid refinement, as:

$$GCI_{1,2} = F_s|E_1| \qquad GCI_{2,3} = F_s|E_1|$$

[1] Roache PJ. *Verification and Validation in Computational Science and Engineering*. Albuquerque, New Mexico, USA: Hermosa, 1998.

[2] Craven BA, Paterson EG, Settles GS, Lawson MJ. *Development and verification of a high-fidelity computational fluid dynamics model of canine nasal airflow*. J Biomech Eng 131: 091002, 2009.

Herein, GCI analysis was performed in terms of:

i. the maximum AV geometric orifice area (GOA_{MAX}) reported at peak systole;
ii. the mean velocity magnitude (V_{mean}) extracted at peak systole from the STJ aortic cross-section, which is an easily recognizable and frequently used landmark in clinical practice to assess aortic flow[3, 4]. STJ is generally uniform in structure, which may facilitate consistent measurements[5], hence providing a clinically recommended and reproducible setting to assess aortic dimension and flow[6, 7, 8];
iii. the peak of maximum principal stress ($\sigma_{I,MAX}$) computed at diastolic peak of transvalvular pressure distinguishing between fused (R-L) and non-coronary (NC) leaflet;
iv. the peak of maximum principal strain ($\varepsilon_{I,MAX}$) computed at diastolic peak of transvalvular pressure distinguishing between fused (R-L) and non-coronary (NC) leaflet.

The comparison of the velocity field between the three tested numerical grids is herein visualized, at peak systole, in terms of: i) *on the left*, velocity magnitude distribution on the STJ cross-section; ii) *in the middle*, 3D wrapped contour of the velocity magnitude in proximity of the aortic valve orifice; iii) *on the right*, instantaneous velocity streamlines on a longitudinal cross-section. As detailed in the figure, there is strong agreement between the fluidynamic results of the medium and fine grids: they both exhibited a very similar BAV ejection jet in terms of velocity magnitude and deflection towards the aortic wall. Similarly, two vortices are visible and highly comparable in terms of localization and extension: the former is located on the left of jet and markedly bigger than the latter, which is positioned on the right of the jet close to the non-coronary sinus.

---

[3] Chai P, Mohiaddin R. *How we perform cardiovascular magnetic resonance flow assessment using phase-contrast velocity mapping*. J Cardiovasc Magn Reson. 2005; 7(4):705-16.

[4] Fratz S, Chung T, Greil GF, Samyn MM, Taylor AM, Valsangiacomo Buechel ER, Yoo SJ, Powell AJ. *Guidelines and protocols for cardiovascular magnetic resonance in children and adults with congenital heart disease: SCMR expert consensus group on congenital heart disease*. J Cardiovasc Magn Reson. 2013; 15:51.

[5] Burman ED, Keegan J, Kilner PJ. *Aortic root measurement by cardiovascular magnetic resonance: specification of planes and lines of measurement and corresponding normal values*. Circ Cardiovasc Imaging. 2008; 1(2):104-13.

[6] Kramer CM, Barkhausen J, Bucciarelli-Ducci C, Flamm SD, Kim RJ, Nagel E. *Standardized cardiovascular magnetic resonance imaging (CMR) protocols: 2020 update*. J Cardiovasc Magn Reson. 2020; 22(1):17.

[7] Schulz-Menger J, Bluemke DA, Bremerich J, Flamm SD, Fogel MA, Friedrich MG, Kim RJ, von Knobelsdorff-Brenkenhoff F, Kramer CM, Pennell DJ, Plein S, Nagel E. *Standardized image interpretation and post-processing in cardiovascular magnetic resonance - 2020 update : Society for Cardiovascular Magnetic Resonance (SCMR): Board of Trustees Task Force on Standardized Post-Processing.* J Cardiovasc Magn Reson. 2020; 22(1):19.

[8] Hundley WG, Bluemke D, Bogaert JG, Friedrich MG, Higgins CB, Lawson MA, McConnell MV, Raman SV, van Rossum AC, Flamm S, Kramer CM, Nagel E, Neubauer S. *Society for Cardiovascular Magnetic Resonance guidelines for reporting cardiovascular magnetic resonance examinations.* J Cardiovasc Magn Reson. 2009; 11:5.

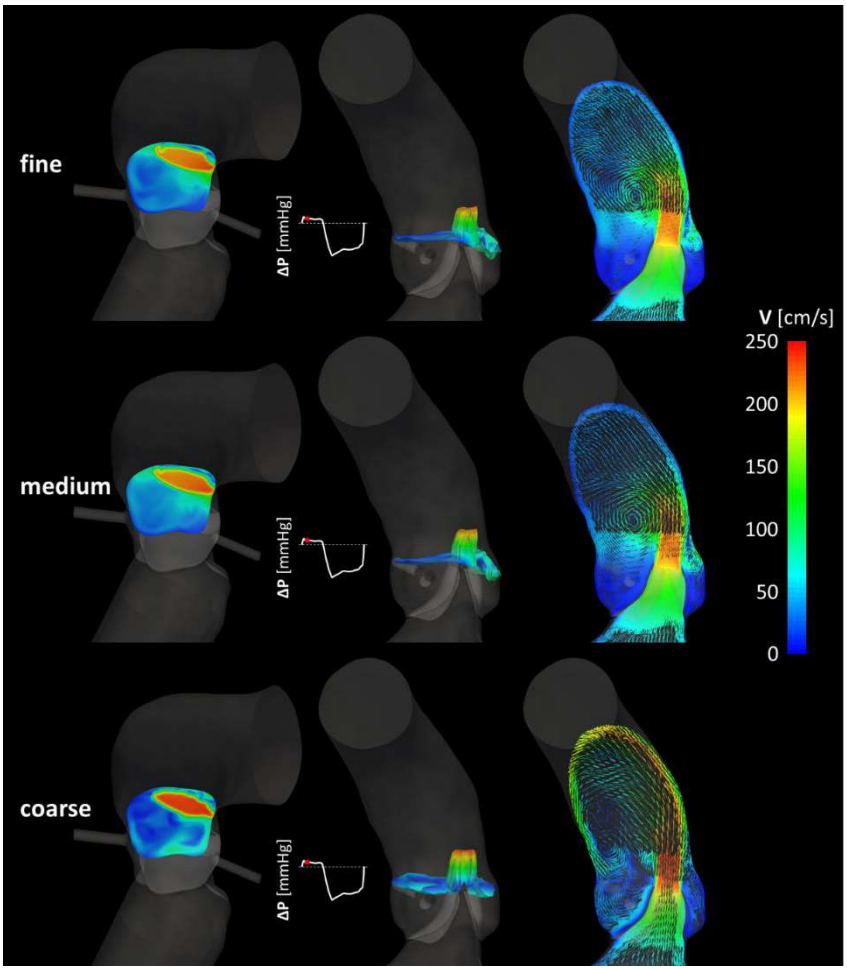

This is even more appreciable, as reported here below, comparing the fine and the medium numerical grids in terms of magnitude of the fluid vorticity vector ($\boldsymbol{\omega}$), which is the curl of the velocity vector, i.e., $\boldsymbol{\omega} = \nabla \times \boldsymbol{v}$.

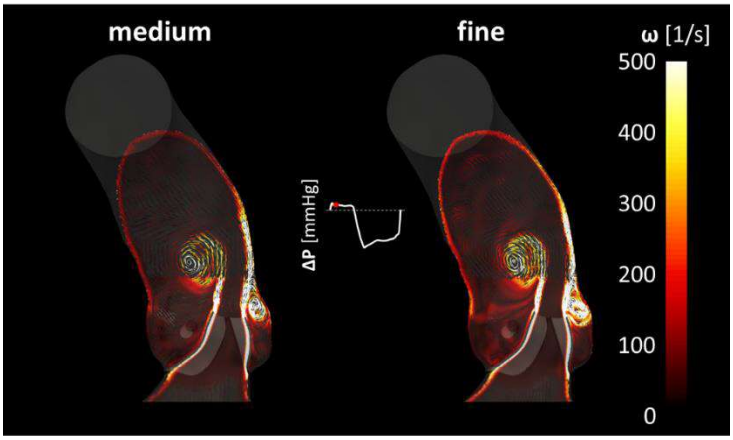

The results of GCI analysis focusing on the structural domain of BAV leaflets are detailed in the following figures. Specifically, the contour maps of σ_I well agree between the different grids on each BAV leaflets; on the non-fused leaflet, $\sigma_{I,MAX}$ increased of 4.7 % from coarse ($\sigma_{I,MAX}$ = 322 kPa) to medium ($\sigma_{I,MAX}$ = 337 kPa) grid and of 0.9 % between medium and fine ($\sigma_{I,MAX}$ = 340 kPa) grid; on the fused leaflet, $\sigma_{I,MAX}$ increased of 7.2% from coarse ($\sigma_{I,MAX}$ = 374 kPa) to medium ($\sigma_{I,MAX}$ = 401 kPa) grid and of 1.7 % between medium and fine ($\sigma_{I,MAX}$ = 408 kPa) grids.

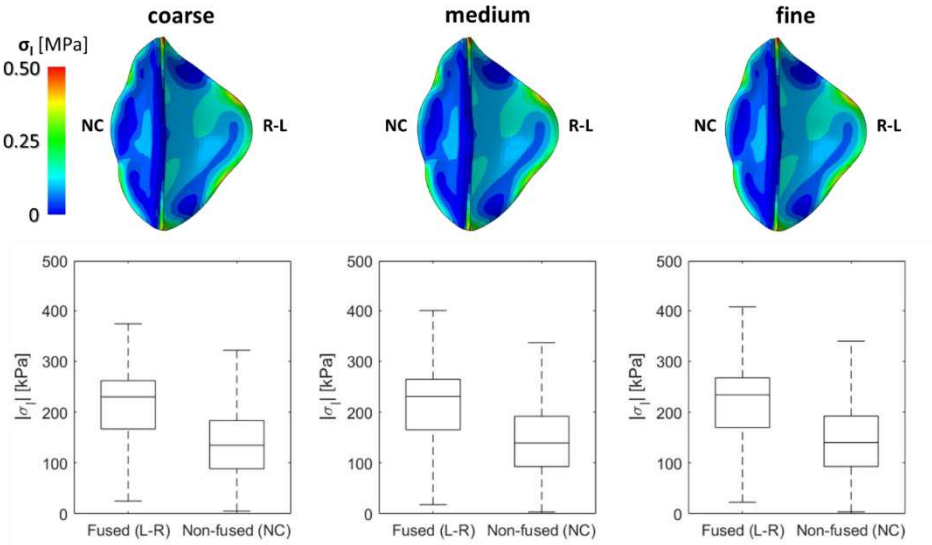

Similarly, good agreement between the grids was also noticed in terms of ε_I contour maps, as reported in the figure below:

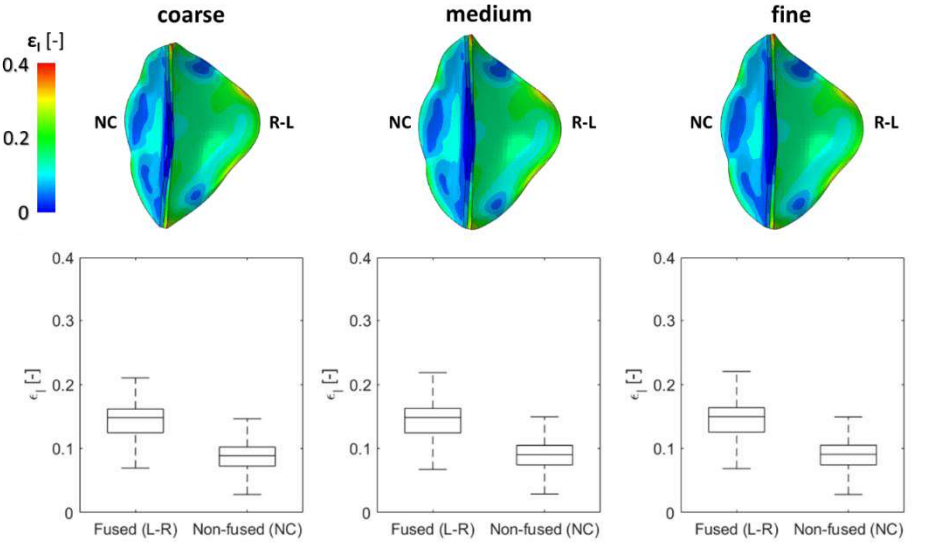

On the non-fused leaflet, $\varepsilon_{I,MAX}$ increased of 2.0 % from coarse ($\varepsilon_{I,MAX}$ = 0.1465) to medium ($\varepsilon_{I,MAX}$ = 0.1495) grid and of 0.3 % between medium and fine ($\varepsilon_{I,MAX}$ = 0.1499) grid; on the fused leaflet, $\varepsilon_{I,MAX}$

increased of 4.0 % from coarse ($\varepsilon_{I,MAX}$ = 0.2101) to medium ($\varepsilon_{I,MAX}$ = 0.2184) grid and of 0.9 % between medium and fine ($\varepsilon_{I,MAX}$ = 0.2203) grids.

All the results are summarized in Table 1, within the body of the manuscript.

B. Comparison between FSI and structural BAV models

Our previous experience[9, 10] clearly indicates that a 2-way FSI coupled model can offer a more thorough strategy to reproduce AV biomechanics, though at a higher computational expense, if compared to a simpler 1-way FSI simulation, which could have served the purpose of solely reproducing the AV fluid dynamics. Indeed, in a previous study[10], we observed differences in AV dynamics, in particular during systole, between the FSI and the structural FEM model of the same aortic root: the structural model reached a wider AV orifice due to a more pronounced outward opening of each AV leaflet that overestimates the clinical scenario. AR stresses and strains, resulting from the FSI model and structural FEM were comparable. Accordingly, following our previous experience, we herein employed a 2-way FSI in order to improve the model realism with respect to ground-truth patient-specific *in vivo* imaging. In order to better appreciate the advantages of 2-way strong FSI model, we compared *in vivo* measurement of the AV geometric orifice area (GOA) against the numerical results of both the 2-way FSI and a purely structural model. In the latter, we simulated AV biomechanics applying the aortic transvalvular pressure drop, defined as the difference between the FSI ventricular and aortic loading pressures, as a uniform distributed load on the ventricular surface of each leaflet. Results are reported in the following figure, highlighting the good agreement between the FSI model and *in vivo* measurements on a *cine* short-axis MRI plane intersecting the leaflets' free-margin.

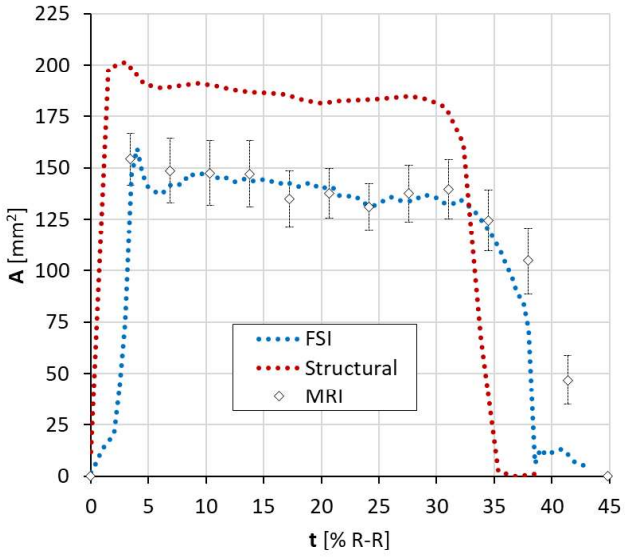

[9] Marom G, Haj-Ali R, Raanani E, Schäfers HJ, Rosenfeld M. *A fluid-structure interaction model of the aortic valve with coaptation and compliant aortic root.* Med Biol Eng Comput. 2012; 50(2):173-82.

[10] Sturla F, Votta E, Stevanella M, Conti CA, Redaelli A. *Impact of modeling fluid-structure interaction in the computational analysis of aortic root biomechanics.* Med Eng Phys. 2013; 35(12):1721-30

As regards the structural model, it reported an overall GOA *overestimation* of about 20÷30% if compared to the FSI model. In addition, it exhibited a more rapid opening and closing phase than FSI model; though AV opening phase was not appreciable *in vivo*, the FSI model proved to better follow the *in vivo* closing phase than the structural model.

Numerical contour plots of AV nodal displacement distribution (U) confirmed the larger orifice reached by the structural model at systole; the Euclidean distance between corresponding nodes on the two grids, reported as box and whiskers plots in the figure below, show maximum distances up to 1.79 mm and 1.15 mm for the fused (R-L) and non-fused (NC) leaflet, respectively.

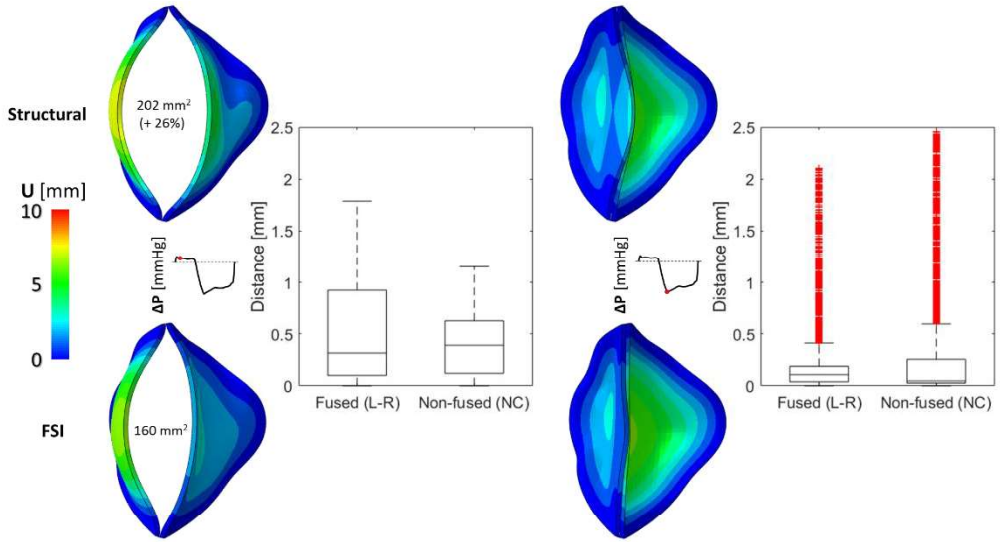

During diastole, the maximum discrepancies, i.e., the maximum distances, were detected close to the leaflet free margin, as clearly depicted in following illustration; reporting a maximum distance of 2.10 mm and 2.46 mm on the fused (R-L) and non-fused (NC) leaflet, respectively.

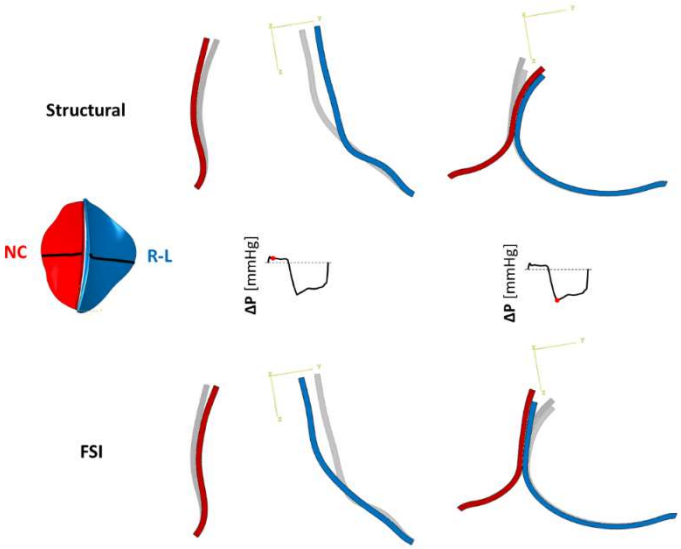

The structural mode, if compared to the FSI model, overestimated $\sigma_{I,MAX}$ distributions on both the AV leaflets though reporting a median increase ($\Delta\sigma_{I,MAX}$) of about 40 kPa (R-L leaflet) and 35 kPa (NC leaflet) at systole; at peak of diastolic transvalvular pressure, the median $\sigma_{I,MAX}$ overestimation decreased to about 21 KPa and 10 kPa on the fused and non-fused leaflet, respectively.

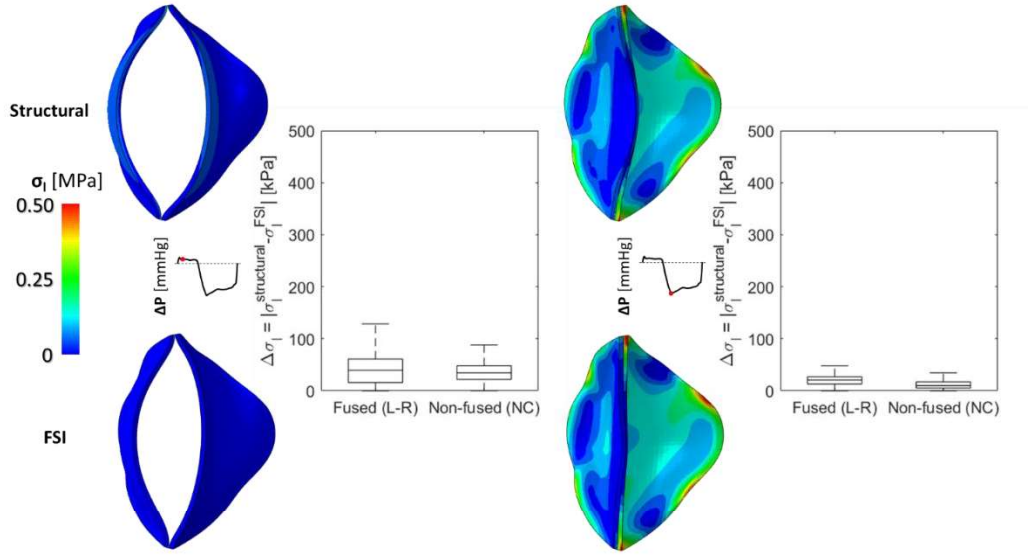

C. Aortic rigid wall

The reason for neglecting aortic wall deformability in the present study is twofold. On the one hand, aortic rigid wall allowed to limit the complexity of the FSI model without taking aortic wall pre-stress into account[11]. On the other hand, patient-specific *in vivo* aortic absolute pressures were not clinically available, neither invasively nor through a non-invasive estimation with a cuff at the arm[12], thus requiring an additional tuning of load boundary conditions to reliably reproduce aortic wall distensibility.

Accordingly, we decided to preliminary assess the impact of aortic wall deformability over the cardiac cycle on the AV biomechanics.

To do so, we evaluated changes in aortic dimensions on a *cine* through-plane velocity-encoded PC-MRI sequence on a plane perpendicular to the aortic valve and localized on the aortic sinotubular junction (STJ), i.e., an easily recognizable landmark where the root joins the tubular portion of the ascending aorta, just above the AV commissures.

STJ is nearly circular in cross section and generally uniform in structure, which may facilitate consistent measurements[13], hence providing a clinically recommended and reproducible setting to assess aortic dimension and flow [14, 15, 16, 17].

As reported in the figure below, we extracted the time-course of the STJ cross-sectional area (A), which was subsequently transformed in the equivalent diameter (D); D reported a maximum systolic value of 30.3 mm and its minimum diastolic value of 28.5 mm, with an overall excursion of 1.8 mm.

---

[11] Votta E, Presicce M, Della Corte A, Dellegrottaglie S, Bancone C, Sturla F, Redaelli A. *A novel approach to the quantification of aortic root in vivo structural mechanics*. Int J Numer Meth Biomed Engng. 2017; 33(9):e2849.

[12] McEniery CM, Cockcroft, JR, Roman MJ, Franklin SS, Wilkinson IB. *Central blood pressure: current evidence and clinical importance*. Eur Heart J 2018; 35:1719-1725.

[13] Burman ED, Keegan J, Kilner PJ. *Aortic root measurement by cardiovascular magnetic resonance: specification of planes and lines of measurement and corresponding normal values*. Circ Cardiovasc Imaging. 2008; 1(2):104-13.

[14] Kramer CM, Barkhausen J, Bucciarelli-Ducci C, Flamm SD, Kim RJ, Nagel E. *Standardized cardiovascular magnetic resonance imaging (CMR) protocols: 2020 update*. J Cardiovasc Magn Reson. 2020; 22(1):17.

[15] Schulz-Menger J, Bluemke DA, Bremerich J, Flamm SD, Fogel MA, Friedrich MG, Kim RJ, von Knobelsdorff-Brenkenhoff F, Kramer CM, Pennell DJ, Plein S, Nagel E. *Standardized image interpretation and post-processing in cardiovascular magnetic resonance - 2020 update : Society for Cardiovascular Magnetic Resonance (SCMR): Board of Trustees Task Force on Standardized Post-Processing.* J Cardiovasc Magn Reson. 2020; 22(1):19.

[16] Fratz S, Chung T, Greil GF, Samyn MM, Taylor AM, Valsangiacomo Buechel ER, Yoo SJ, Powell AJ. *Guidelines and protocols for cardiovascular magnetic resonance in children and adults with congenital heart disease: SCMR expert consensus group on congenital heart disease*. J Cardiovasc Magn Reson. 2013; 15:51.

[17] Hundley WG, Bluemke D, Bogaert JG, Friedrich MG, Higgins CB, Lawson MA, McConnell MV, Raman SV, van Rossum AC, Flamm S, Kramer CM, Nagel E, Neubauer S. *Society for Cardiovascular Magnetic Resonance guidelines for reporting cardiovascular magnetic resonance examinations.* J Cardiovasc Magn Reson. 2009; 11:5.

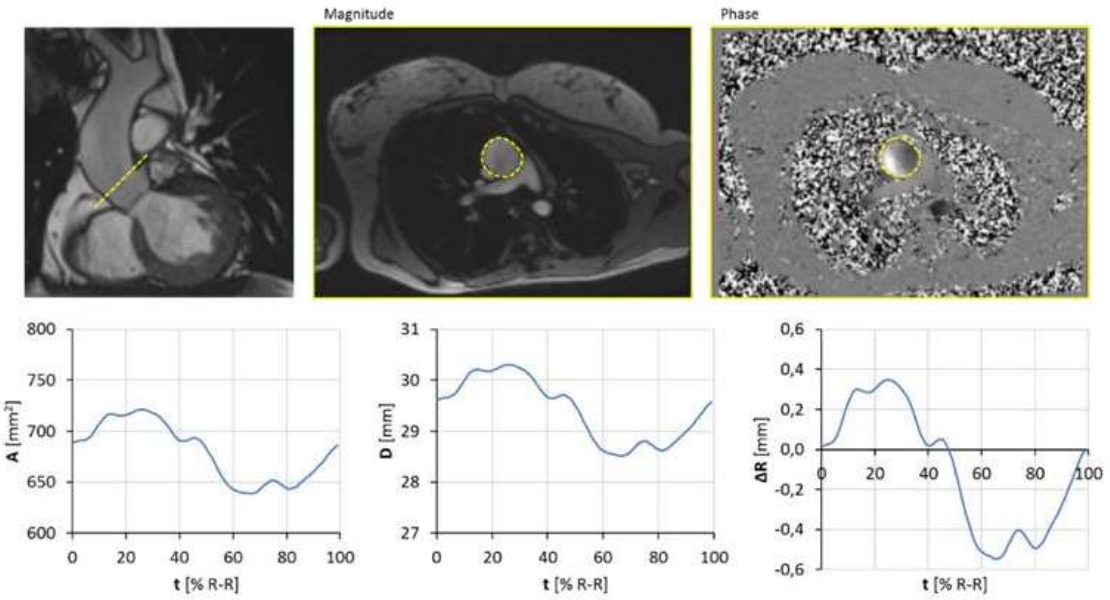

Such a time-dependent variation was prescribed, in a structural simulation, as boundary condition of radial displacement (ΔR) to the nodes lying on each AV leaflet attachment profile, thus reproducing *in vivo* systolic enlargement and diastolic contraction of the aortic root wall.

We compared the results of the analysis against the corresponding structural simulation of AV biomechanics under aortic wall rigid conditions. Differences proved to be almost negligible in terms of nodal displacements (U) at both systole and diastole, with overall Euclidean nodal distances between the grids below 0.05 mm, as detailed in the following illustration.

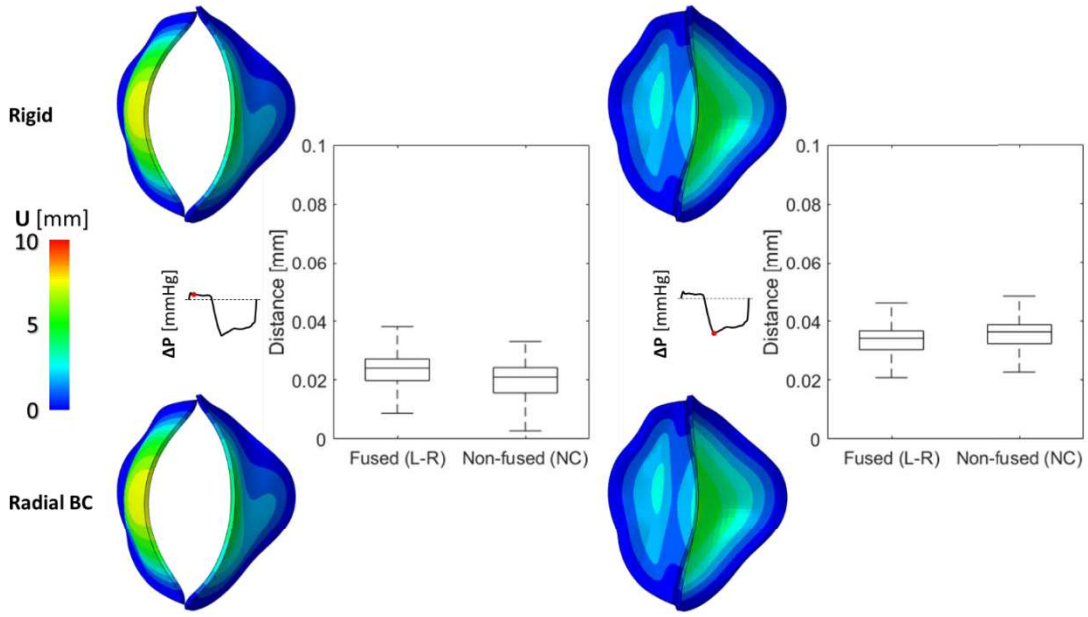

We also compared the two simulations in terms of $\sigma_{I,MAX}$ distribution and $\Delta\sigma_{I,MAX}$ noticing, when simulating AV biomechanics taking dimensional changes into account, a median $\sigma_{I,MAX}$ increase of about 3 kPa and 4 kPa in the fused and non-fused AV leaflet, respectively.

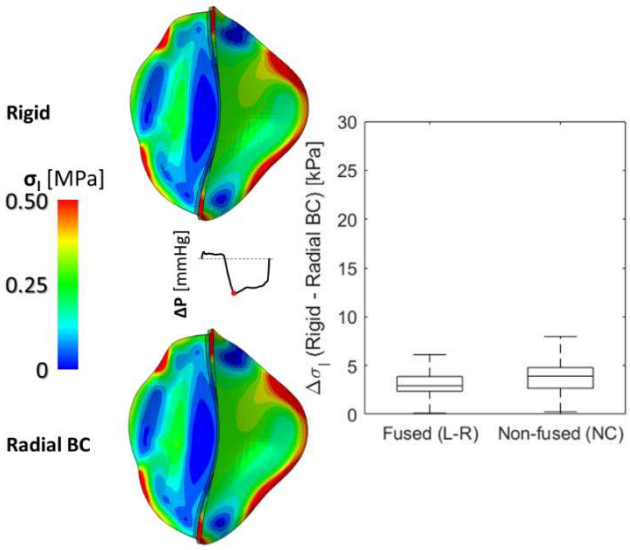

D. Mechanical response of BAV leaflets - Anisotropy

AV cusps' fiber orientation was not taken into account since patient-specific quantification of AV fibers structure was not possible. Instead, the native AV leaflets were modelled with isotropic and hyperelastic properties as used previously by our and other groups[18, 19, 20].

Nonetheless, since the fibers are the load bearing structure of AV leaflets, we estimated through a preliminary structural simulation the impact that this approximation may have on AV biomechanics. To do so, AV mechanical hyperelastic anisotropy was modelled fitting *ex vivo* circumferential and radial biaxial data[21] using the transversely anisotropic and hyperelastic strain energy function (U) originally proposed by Guccione *et al.*[22]:

$$U = \frac{C}{2}(e^{Q} - 1) + K\left(\frac{J^2 - 1}{2} - \ln J\right)$$

where C is the first constitutive parameter, J the determinant of the deformation gradient tensor, K the bulk modulus Q has the form:

$$Q = 2b_1 tr(E) + b_2 E_{ff}^2 + b_3(E_{ss}^2 + E_{nn}^2 + E_{sn}^2 + E_{ns}^2) + b_4\left(E_{nf}^2 + E_{fn}^2 + E_{fs}^2 + E_{sf}^2\right)$$

with E_{ij} being the components of the Green-Lagrange strain tensor, expressed with reference to a coordinate system whose f, s, n axes are aligned with each AV leaflet commissure-commisure, annulus-to-free margin and through thickness direction, respectively; b_1, b_2, b_3, b_4 are the remaining constitutive parameters. The result of fitting is reported in the following figure for non-fused (NC, R^2=0.9983) and fused (R-L, R^2=0.9995) leaflet in the circumferential (i.e., commissure-to-commissure) and radial (i.e., annulus-to-free margin) directions.

---

[18] Ghosh RP, Marom G, Bianchi M, D'souza K, Zietak W, Bluestein D. *Numerical evaluation of transcatheter aortic valve performance during heart beating and its post‐deployment fluid–structure interaction analysis*. Biomech Model Mechanobiol. 2020 *In Press*.

[19] Bianchi M, Marom G, Ghosh RP, Rotman OM, Parikh P, Gruberg L, Bluestein D. *Patient-specific simulation of transcatheter aortic valve replacement: impact of deployment options on paravalvular leakage*. Biomech Model Mechanobiol. 2019; 18(2):435-451.

[20] Cao K, Sucosky P. *Computational comparison of regional stress and deformation characteristics in tricuspid and bicuspid aortic valve leaflets.* Int J Numer Method Biomed Eng. 2017; 33(3).

[21] Martin C. Sun W. *Biomechanical characterization of aortic valve tissue in humans and common animal models*. J Biomed Mater Res A. 2012; 100(6):1591-9

[22] Guccione JM, McCulloch AD, Waldman LK. *Passive material properties of intact ventricular myocardium determined from a cylindrical model*. J Biomech Eng. 1991; 113(1):42-55.

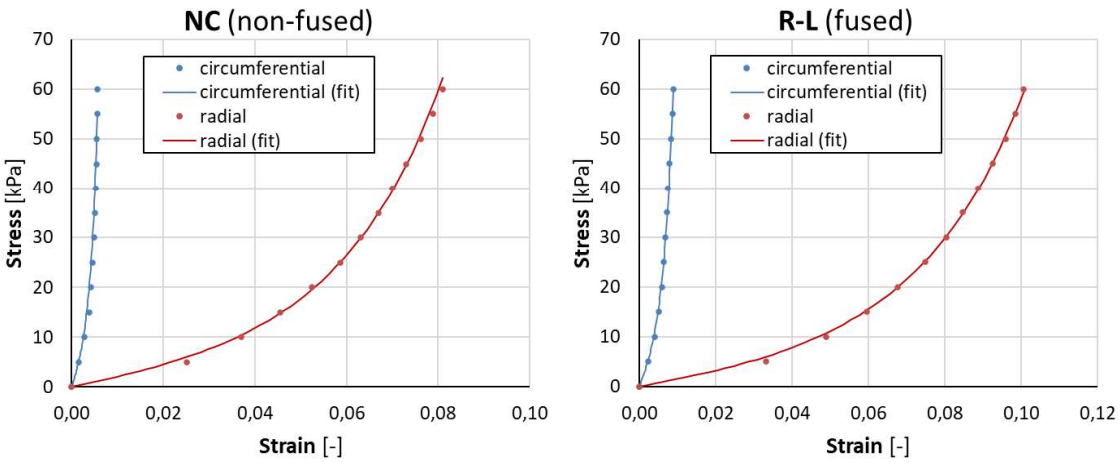

The following constitutive parameters were used:

Leaflet	C [MPa]	b_1 [-]	b_2 [-]	b_3 [-]	b_4 [-]	K [MPa]
NC (non-fused)	$2.33 \cdot 10^{-3}$	$3.45 \cdot 10^{-3}$	$1.30 \cdot 10^{3}$	85.6	0.0	50.0
R-L (fused)	$2.72 \cdot 10^{-3}$	$1.55 \cdot 10^{-6}$	$7.70 \cdot 10^{2}$	54.0	0.0	50.0

We compared these preliminary numerical results, between isotropic hyperelastic and transversely anisotropic hyperelastic models in terms of nodal displacement (U) and maximum principal stress ($\sigma_{I,MAX}$) experienced by AV leaflets, at both systole and diastole.

Contour plots of AV nodal displacement distribution are reported here below for each simulation, during systole (on the left) and during diastole (on the right).

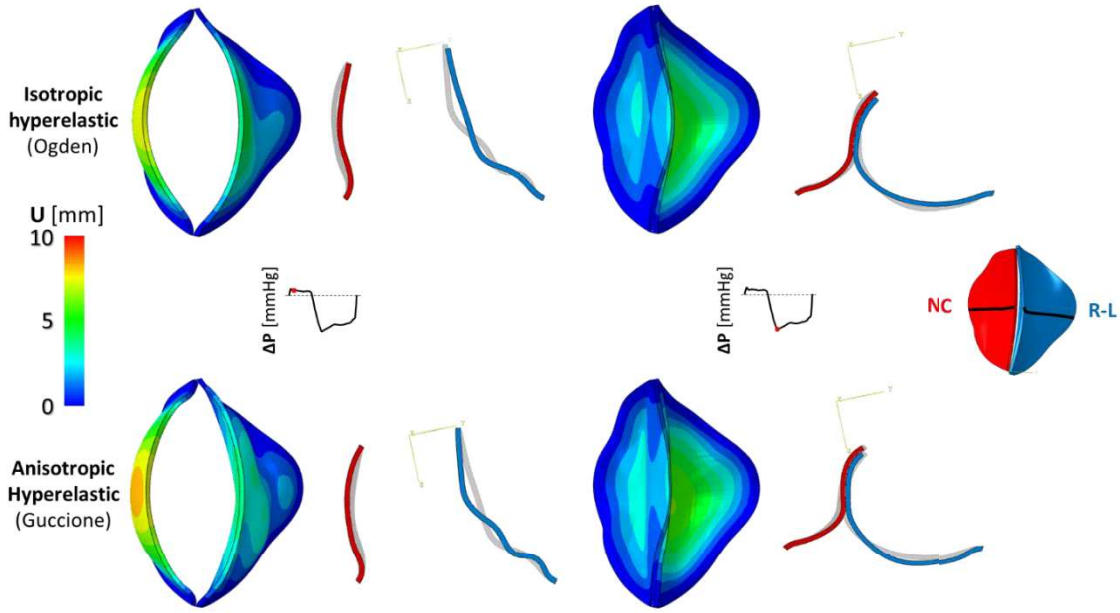

Nodal distances, computed as the Euclidean distance between corresponding nodes on the two grids, are reported as box and whiskers plots showing at systole a median distance of 0.48 mm and 0.51 mm for the fused (R-L) and non-fused (NC), respectively.

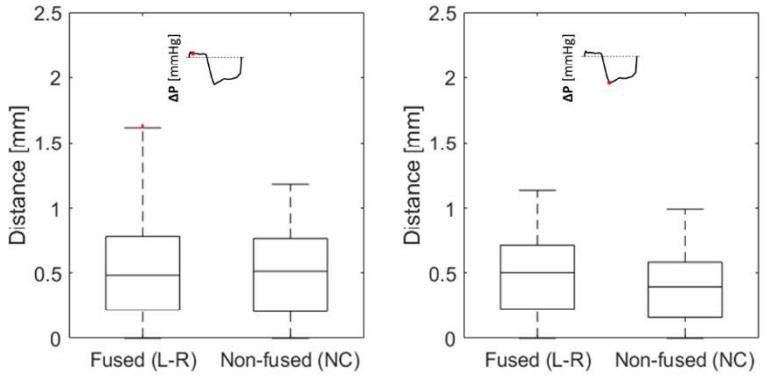

Of note, as visible from the longitudinal cut-view cutting each AV leaflet along its belly, the highest discrepancies were detected along the fused leaflet (blue profile in figure) with localized distances between the two grids increasing up to 1.64 mm. At peak of diastolic transvalvular pressures, median distances were equal to 0.51 mm and 0.40 mm for the fused (R-L) and non-fused (NC) leaflet, respectively.

Contour maps of $\sigma_{I,MAX}$ distribution are reported below for both the simulations and mechanical stress differences ($\Delta\sigma_{I,MAX}$) between anisotropic and isotropic models pointed out by means of box and whiskers plots.

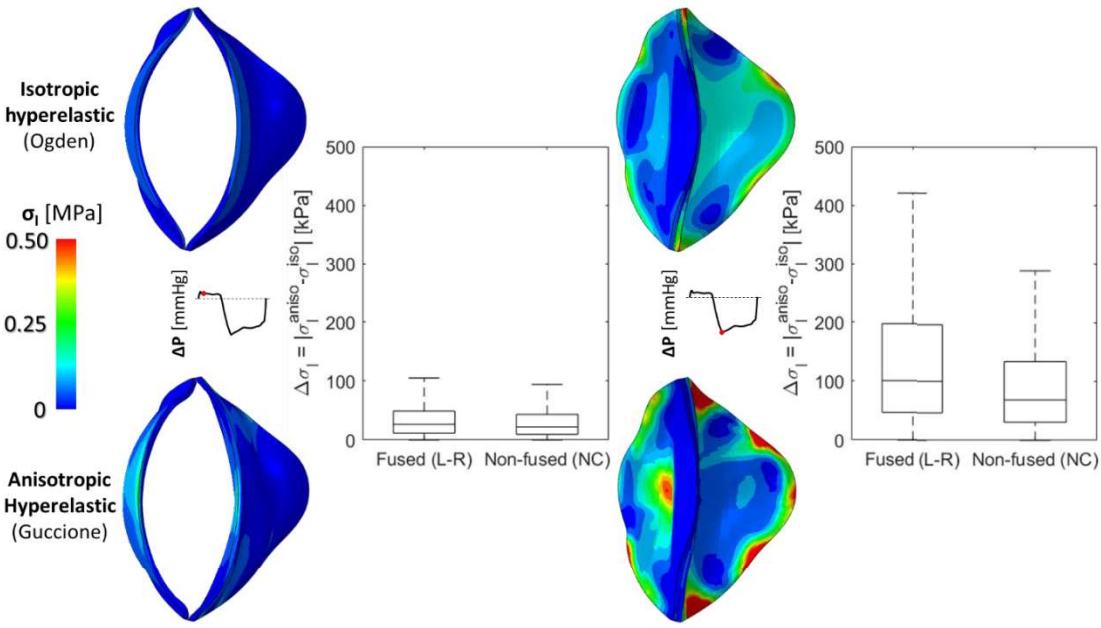

The anisotropic model reported increased $\sigma_{I,MAX}$ values: at systole, median differences were equal to 26.5 kPa and 22.2 kPa on the fused and non-fused leaflet while at peak of transvalvular diastolic pressure, median $\Delta\sigma_{I,MAX}$ increased up to 100.7 kPa and 68.9 kPa, respectively.

Supplementary figures

Figure S1.

Regional subdivision of each BAV leaflet, i.e., fused (L-R) and non-fused (NC), into i) belly, ii) coaptation, iii) attachment and iv) free margin sectors.

Supplementary videos

Online Video 1.

4D Flow analysis of BAV-related hemodynamics in the ascending aorta.

Supplementary tables

Table S1. Regional σ_I distribution averaged on BAV leaflets during systole.

Leaflet region	Fused (R-L)		Non-fused (NC)		P-value[a]	P-value[b]	P-value[c]
	Fibrosa	Ventricularis	Fibrosa	Ventricularis			
Belly	-4.37 (-5.13, -0.30)	-5.87 (-8.13, -4.37)	-3.01 (-4.32, 4.86)	-1.63 (-3.15, 4.36)	0.7648	0.0005	0.9361
Coaptation	-1.70 (-5.30, 2.23)	-7.67 (-8.54, -5.43)	2.60 (-3.63, 11.27)	-8.62 (-9.16, -5.69)			
Attachment	-15.91 (-16.22, -4.90)	1.26 (-5.77, 8.42)	-24.05 (-31.01, -16.75)	28.93 (12.42, 59.71)			
Free margin	-7.36 (-8.03, -5.90)	-7.82 (-8.84, -6.74)	4.33 (3.41, 13.99)	3.22 (2.10, 14.67)			

Systolic σ_I data expressed in Pa as median (25^{th}, 75^{th} percentile);
[a] fibrosa *vs.* ventricularis leaflet surface (Wilcoxon matched-pair signed rank test);
[b] fused *vs.* non-fused leaflet (Wilcoxon matched-pair signed rank test);
[c] between leaflets regions (Friedman test).

Table S2. Regional σ_I distribution averaged on BAV leaflets during diastole.

Leaflet region	Fused (R-L)		Non-fused (NC)		P-value[a]	P-value[b]	P-value[c]
	Fibrosa	Ventricularis	Fibrosa	Ventricularis			
Belly	174.2 (155.4, 181.6)	194.6 (174.8, 202.3)	105.2 (95.4, 108.9)	127.0 (116.0, 131.3)	0.0038	<0.0001	<0.0001
Coaptation	156.2 (140.7, 162.5)	160.5 (144.6, 166.0)	25.8 (23.2, 26.8)	22.9 (20.8, 23.7)			
Attachment	258.7 (233.2, -369.4)	47.6 (39.8, 50.2)	217.5 (199.9, -225.0)	-13.2 (-14.2, -12.6)			
Free margin	155.7 (141.3, 161.5)	131.2 (118.4, 137.0)	39.1 (37.7, 43.0)	35.7 (33.3, 36.1)			

Diastolic σ_I data expressed in Pa as median (25^{th}, 75^{th} percentile);
[a] fibrosa *vs.* ventricularis leaflet surface (Wilcoxon matched-pair signed rank test);
[b] fused *vs.* non-fused leaflet (Wilcoxon matched-pair signed rank test);
[c] between leaflets regions (Friedman test).

Table S3. Regional WSS distribution averaged on BAV leaflets during systole.

Leaflet region	Fused (R-L)		Non-fused (NC)		P-value[a]	P-value[b]	P-value[c]
	Fibrosa	Ventricularis	Fibrosa	Ventricularis			
Belly	0.37 (0.20, 0.90)	2.60 (1.69, 6.44)	5.08 (2.48, 5.57)	6.86 (5.99, 11.02)	< 0.0001	< 0.0001	< 0.0001
Coaptation	0.72 (0.67, 3.40)	7.51 (3.49, 13.04)	4.52 (4.04, 6.10)	8.52 (6.80, 13.63)			
Attachment	0.10 (0.06, 0.52)	1.36 (0.54, 3.55)	2.00 (1.21, 2.63)	3.82 (2.58, 9.14)			
Free margin	1.12 (0.89, 7.19)	12.65 (9.92, 18.82)	5.30 (4.28, 6.42)	14.64 (11.15, 21.60)			

Systolic WSS data expressed in Pa as median (25^{th}, 75^{th} percentile);
[a] fibrosa *vs.* ventricularis leaflet surface (Wilcoxon matched-pair signed rank test);
[b] fused *vs.* non-fused leaflet (Wilcoxon matched-pair signed rank test);
[c] between leaflets regions (Friedman matched test).

Table S4. Regional WSS distribution averaged on BAV leaflets during diastole.

Leaflet region	Fused (R-L)		Non-fused (NC)		P-value[a]	P-value[b]	P-value[c]
	Fibrosa	Ventricularis	Fibrosa	Ventricularis			
Belly	1.33 (0.98, 1.95)	1.32 (0.82, 4.35)	1.17 (0.53, 1.52)	1.10 (0.70, 2.54)	0.3494	0.0011	< 0.0001
Coaptation	0.69 (1.4, 1.89)	0.69 (0.11, 1.08)	1.91 (1.48, 3.03)	1.67 (1.45, 2.70)			
Attachment	0.75 (0.44, 1.04)	0.46 (0.22, 1.62)	0.67 (0.28, 0.97)	0.72 (0.47, 3.89)			
Free margin	2.74 (1.81, 3.87)	1.93 (1.15, 2.85)	2.67 (1.92, 4.69)	3.56 (3.22, 7.47)			

Diastolic WSS data expressed in Pa as median (25^{th}, 75^{th} percentile);
[a] fibrosa *vs.* ventricularis leaflet surface (Wilcoxon matched-pair signed rank test);
[b] fused *vs.* non-fused leaflet (Wilcoxon matched-pair signed rank test);
[c] between leaflets regions (Friedman matched test).